CLEAR: Paschen-β Star Formation Rates and Dust Attenuation of Low Redshift Galaxies

Nikko J. Cleri [iD],[1] Jonathan R. Trump [iD],[1] Bren E. Backhaus [iD],[1] Ivelina Momcheva [iD],[2] Casey Papovich [iD],[3, 4]
Raymond Simons [iD],[2] Benjamin Weiner [iD],[5] Vicente Estrada-Carpenter [iD],[3, 4] Steven L. Finkelstein [iD],[6]
Mauro Giavalisco,[7] Zhiyuan Ji [iD],[8] Intae Jung [iD],[9, 10] Jasleen Matharu [iD],[3, 4] and Megan R. Sturm [iD][1]

[1]Department of Physics, University of Connecticut, Storrs, CT 06269, USA
[2]Space Telescope Science Institute, 3700 San Martin Drive, Baltimore, MD, 21218 USA
[3]Department of Physics and Astronomy, Texas A&M University, College Station, TX, 77843-4242 USA
[4]George P. and Cynthia Woods Mitchell Institute for Fundamental Physics and Astronomy, Texas A&M University, College Station, TX, 77843-4242 USA
[5]MMT/Steward Observatory, 933 N. Cherry St., University of Arizona, Tucson, AZ 85721, USA
[6]Department of Astronomy, The University of Texas, Austin, Texas, 78712 USA
[7]Astronomy Department, University of Massachusetts, Amherst, MA, 01003 USA
[8]Department of Astronomy, University of Massachusetts Amherst, 710 N. Pleasant St., Amherst, MA, 01003, USA
[9]Department of Physics, The Catholic University of America, Washington, DC 20064, USA
[10]Astrophysics Science Division, Goddard Space Flight Center, Greenbelt, MD 20771, USA

ABSTRACT

We use Paβ (1282 nm) observations from the Hubble Space Telescope (*HST*) G141 grism to study the star formation and dust attenuation properties of a sample of 32 low redshift ($z < 0.287$) galaxies in the CLEAR survey. Many of the galaxies in the sample have significantly higher Paβ emission than expected from the star formation rates (SFRs) measured from their (attenuation-corrected) UV continuum or Hα emission, suggesting that Paβ is revealing star formation that is otherwise hidden within gas that is optically thick to UV-continuum and Balmer line emission. Galaxies with lower stellar mass tend to have more scatter in their ratio of Paβ to attenuation-corrected UV SFRs. When considering our Paβ detection limits, this observation is consistent with burstier star formation histories in lower mass galaxies. We also find a large amount of scatter between the nebular dust attenuation measured by Paβ/Hα and Hα/Hβ, implying that the Balmer decrement underestimates the attenuation in galaxies across a broad range of stellar mass, morphology, and observed Balmer decrement. Comparing the nebular attenuation from Paβ/Hα with the stellar attenuation inferred from the spectral energy distribution, our galaxies are consistent with an average stellar to nebular ratio of 0.44, but with a large amount of excess scatter beyond the observational uncertainties. Together, these results show that Paβ is a valuable tracer of a galaxy's star formation rate, often revealing star formation that is otherwise missed by UV and optical tracers.

1. INTRODUCTION

Star formation rates (SFRs) are a critical quantity in the understanding of galaxy evolution. There exist several different methods of estimating SFR in a given galaxy, the most direct of which is counting identifiable stars of a specific age. With current instrumentation, this method of star counting is limited to the most immediate of Milky Way satellites. In more distant galaxies, the primary methods of measuring SFRs are using continuum and emission-line tracers (e.g., Kennicutt & Evans 2012).

Near-ultraviolet (UV) continuum observations of a galaxy measure the photospheric emission of massive young stars that formed within the last 10-200 Myr, and so the UV continuum acts as a direct tracer of recent star formation (Kennicutt & Evans 2012). However, UV continuum observations are highly sensitive to attenuation by interstellar dust. In principle, this attenuation can be corrected using the UV slope β, but in practice the unknown intrinsic UV slope and differences in the UV shape of different attenuation laws complicate this approach (e.g., Salim & Narayanan 2020). Another approach is to add the reprocessed IR emission to the observed UV continuum for a "ladder" SFR (Wuyts et al. 2011), but this is similarly complicated by UV optical depth effects and/or potential anisotropy of the IR emission.

Optical and near-infrared (IR) emission lines from ionized gas around massive stars are also widely used as SFR indicators. These emission lines receive peak contribution from stars of mass 30-40 M$_\odot$, and as such are tracers of stars with lifetimes of 3-10 Myr. Recombination lines of hydrogen are especially useful to trace star formation since they are insensitive to metallicity and relatively insensitive to gas temperature and density (Osterbrock 1989). Since the continuum and emission-line tracers correspond to different timescales, their ratio can be used to measure the burstiness of the star

formation (e.g., Guo et al. 2016; Weisz et al. 2012). Still, optical emission lines are susceptible to dust attenuation. For example, Hα flux is reduced by a factor of $\sim$2 at a modest attenuation of $A_V = 1$, and reduced by a factor of $\sim$10 in a dusty galaxy with $A_V = 3$. The Balmer decrement (Hα/Hβ) can be used to correct for the attenuation, but this correction saturates at high attenuation and can be inaccurate if the emission and/or attenuation scales are smaller than the resolution. Uncertainties in correcting for dust attenuation fundamentally limits measurements of star formation burstiness from the UV continuum and optical emission-line SFR tracers (Broussard et al. 2019).

Near-IR recombination lines of hydrogen offer a solution to the problem of dust attenuation in measuring SFR. Just like the more commonly used Balmer series, the Paschen lines of hydrogen are highly sensitive to the ionizing ($E > 13.6$ eV) radiation of OB stars formed with the last $<$10 Myr, while remaining relatively insensitive to nuisance parameters like the temperature and density of the star-forming gas (Osterbrock 1989). But unlike the optical Balmer lines, the near-IR Paschen lines are far less affected by interstellar dust extinction, and so they can reveal otherwise hidden star-forming regions that are shrouded in gas and dust that is optically thick to Balmer emission. Previous work has used the Paα (18750Å) emission line to calibrate mid-IR SFR indicators in nearby starburst and luminous IR galaxies (Alonso-Herrero et al. 2006; Calzetti et al. 2007) and in rare lensed galaxies at higher redshift (Papovich et al. 2009; Finkelstein et al. 2011; Shipley et al. 2016).

In this work we study Paβ (1282 nm), the $n = 5 \rightarrow 3$ hydrogen recombination line, as an SFR indicator. We use Paβ fluxes measured from near-IR spectroscopy from the *HST*/WFC3 grisms taken as part of the 3D-HST (Momcheva et al. 2016) and CLEAR (Simons et al. in prep.) surveys, as described in Section 2. In Section 3, we compare with Paβ with other SFR indicators, demonstrating that Paβ includes star formation missed by UV and optical tracers and showing tentative evidence for burstier star formation at low mass. Section 4 discusses the use of Paβ/Hα as an alternative attenuation indicator to the Balmer decrement or V-band continuum attenuation. We summarize our results and discuss future applications with *JWST* in Section 5.

Throughout this work, we assume a WMAP9 cosmology with $\Omega_{m,0} = 0.287$, $\Omega_{\Lambda,0} = 0.713$, and $H_0 = 69.3$ km s^{-1} Mpc^{-1} (Hinshaw et al. 2013). We also assume intrinsic line ratios of Hα/Hβ = 2.86 and Hα/Paβ = 17.6, corresponding to Case B recombination at a temperature of $T = 10^4$ K and a density of $n_e = 10^4$ cm^{-3} (Osterbrock 1989).

2. DATA

Our data come from the CLEAR survey (a Cycle 23 *HST* program, PI: Papovich), which consists of deep (12-orbit depth) *HST*/WFC3 G102 slitless grism spectroscopy covering $0.8 - 1.2$ μm within 12 fields split between the GOODS-North (GN) and GOODS-South (GS) extragalactic survey fields (Estrada-Carpenter et al. 2019, Simons et al. in prep.). The CLEAR pointings overlap with the larger 3D-HST survey area (Momcheva et al. 2016), which provides slitless G141 grism spectra of 2-orbit depth and a spectral wavelength range of 1.1-1.65 μm.

### 2.1. *G102 and G141 Spectroscopy, Redshifts and Line Fluxes*

The grizli (grism redshift and line analysis) pipeline[1] serves as the primary method of data reduction for the CLEAR dataset. In contrast to traditional methods of extracting one-dimensional (1D) spectra from slit observations, grizli directly fits the two-dimensional (2D) spectra with model spectra convolved to the galaxy image and for multiple position angles of grism observations. This process yields complete and uniform characterization of the suite of spectral line features of all objects observed in each of the G102 and G141 grisms. The most relevant of these spectral properties for our analysis are redshifts, line fluxes, and emission-line maps. The Paβ line is not included in the grizli fits by default, but was included in the CLEAR reductions for this work.

The redshifts and Paβ line fluxes for the objects in our sample are taken from the CLEAR release v2.1.0 (Simons et al. in prep.). We note that 17 of the objects in our sample have matching spectroscopic redshifts from ground-based programs (as compiled in the 3D-HST catalog), and another 6 have a redshift from well-detected Hα in the G102 grism.

2.2. *Parent Dataset and Sample Selection*

We selected a sample of Paβ-emitting galaxies from the CLEAR parent catalog by first requiring $z < 0.287$, such that Paβ is within the observed-frame spectral range and blueward of the G141 sensitivity decline at 1.65 μm. The CLEAR extractions are limited to galaxies with $m_{F105W} < 25$. We additionally required a reliable spectroscopic redshift and a detected Paβ emission line. For sources without existing redshifts, we require Paβ signal-to-noise (SNR) of SNR > 3: this selects 21 CLEAR galaxies. We additionally include 11 galaxies with reliable spectroscopic redshifts from other lines (from either ground-based optical spectroscopy or from Hα emission in the G102 spectrum) that have Paβ detected with SNR > 1. This combined selection ensures reliable redshifts, either from a high-SNR Paβ detection or from other (brighter) emission lines, while remaining as inclusive as possible to non-spurious Paβ emission. Our sample includes

---

[1] https://github.com/gbrammer/grizli/
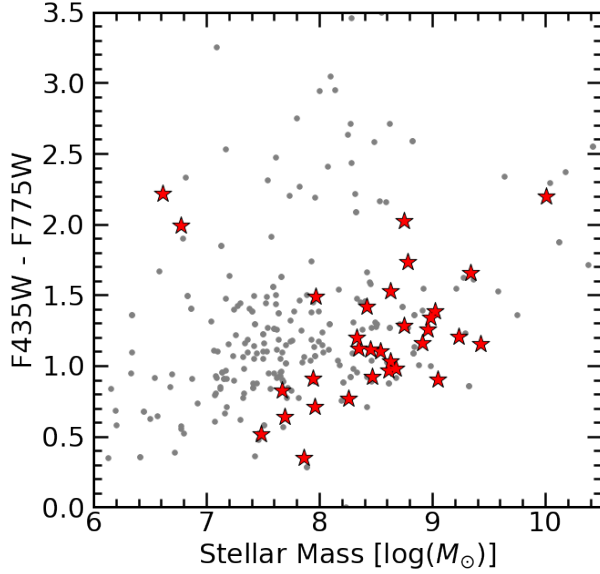
Figure 1. The relation between F435W-F775W color and stellar mass for galaxies of redshift $z < 0.287$. Our sample is shown as red stars, with the rest of the CLEAR galaxies in this redshift range shown as gray points. The galaxies in our sample are broadly representative of the population of $z < 0.287$ star-forming galaxies with $\log(M_*/M_\odot) \gtrsim 7.5$. The sample of Pa$\beta$-detected galaxies also includes a few red galaxies that are likely dust-obscured (see Section 4).

a total of 32 Paβ-emitting galaxies and comprises approximately 11% of all CLEAR galaxies in this redshift range.

Figure 1 shows the color-mass relation for the galaxies in our sample (in red) with respect to all CLEAR galaxies in the redshift range $z < 0.287$ (in gray). The F435W and F775W magnitudes and stellar masses are taken from the CANDELS/SHARDS multiwavelength catalog (Barro et al. 2019). Our galaxy sample is broadly representative of the larger galaxy population in CLEAR, with some preference for blue galaxies with $\log(M_*/M_\odot) \gtrsim 7.5$.

Figure 2 shows F435W, F606W, F105W (in GOODS-N) , and F125W direct images of all 32 galaxies in our sample. Our sample includes a broad range of galaxy morphologies, including extended disks, bright compact sources, and diffuse irregular objects. The complete figure set of multi-band direct images for all 32 galaxies in the sample is available in the online journal.

Figure 3 shows one-dimensional (1D) and two-dimensional (2D) spectra for all 32 galaxies in our sample. The CLEAR catalog has 2D spectra for each position angle (PA) at which an object is observed. The complete figure set of 1D and 2D spectra for all 32 galaxies in the sample is available in the online journal.

2.3. *Photometry and Derived Quantities*
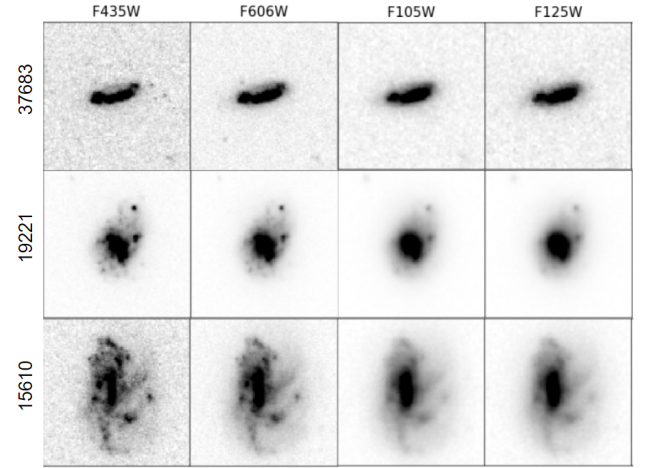
Figure 2. *HST* F435W, F606W, F105W (in GOODS-N), and F125W direct images of the galaxies in our sample. Each image is $3''$ on each side. Our sample includes a diverse range of galaxy morphologies. The complete figure set of multi-band images for all galaxies in the sample is available in the online journal.
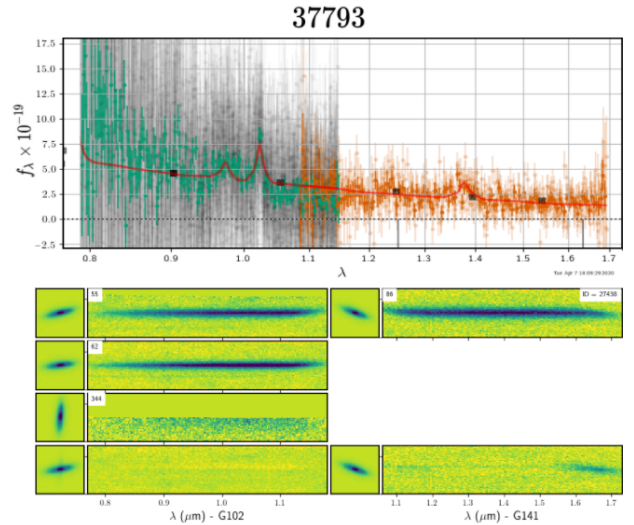
Figure 3. Rest frame one-dimensional (1D) and two-dimensional (2D) spectra for a galaxy in our sample. The G102 spectrum is shown at left (green) and the G141 spectrum at right (orange), with uncertainties in the 1D fluxes shown in gray. The figure shows 2D spectra for each position angle (PA) at which an object is observed, with the *HST* ORIENT given in each panel. The F105W (G102) and F140W (G141) direct images included show the relative PA as indicated by the ORIENT. The composite continuum-subtracted 2D spectra are shown in the bottom row. Paβ is present at 1.282 μm in the rest-frame spectra. The complete figure set of 1D and 2D spectra for all 32 galaxies in the sample is available in the online journal.

We take stellar masses for objects in our sample from the 3D-HST catalog (Skelton et al. 2014), derived from the CANDELS photometry (Grogin et al. 2011; Koekemoer et al. 2011). The stellar masses are calculated with FAST (Kriek

et al. 2009), using a Bruzual & Charlot (2003) stellar population synthesis model library, a Chabrier (2003) IMF, solar metallicity, and assuming exponentially declining star formation histories. The stellar masses of our $z < 0.287$ galaxies are generally robust to these assumptions because the peak of the stellar emission is well-constrained by the high-quality CANDELS near-IR imaging. We additionally use the V-band attenuation (A_V) measured from the same FAST fit to the spectral energy distribution.

We use UV continuum SFRs from the catalog of Barro et al. (2019), which supplements the CANDELS multiwavelength data with SHARDS photometry (Pérez-González et al. 2013) in GOODS-N. Attenuation-corrected UV SFRs are calculated using the Kennicutt (1998) calibration with a dust attenuation correction (Barro et al. 2019):

$$SFR_{UV}^{corr}[M_\odot yr^{-1}] = (1.09 \times 10^{-10})(10^{0.4A_{280}})(3.3L_{280}/L_\odot) \quad (1)$$

L_{280} and A_{280} are the UV luminosity and dust attenuation at rest-frame $\lambda = 280$ nm, respectively. The UV luminosity $L_{280} \equiv \nu L_\nu(2800\text{Å})$ is calculated from EAZY with a best-fit spectral energy distribution (Brammer et al. 2008; Wuyts et al. 2011). The UV attenuation is inferred iteratively, using the UV slope β measured from the best-fit SED while ensuring consistency with the IR (non)detection and the star formation mass sequence (see Appendix D of Barro et al. 2019).

UV + IR "ladder" SFRs are calculated for objects with mid/far-IR detections following Wuyts et al. (2011):

$$SFR_{UV+IR}[M_\odot yr^{-1}] = 1.09 \times 10^{-10}(L_{IR} + L_{2800})L_\odot \quad (2)$$

The relative scale of the UV and IR contribution is based on local universe calibrations (Kennicutt & Evans 2012), and the overall scale assumes a Chabrier (2003) initial mass function. The UV + IR ladder SFR ultimately measures the UV continuum emission that is not attenuated by dust plus the reprocessed IR continuum emission from the UV which were attenuated by the dust.

Our galaxies have morphology measurements from van der Wel et al. (2012). We use effective (50% light) radii and Sérsic (1968) indices for galaxies with "good" GALFIT (Peng et al. 2010) fits with flag = 0 (see van der Wel et al. 2012 for details).

2.4. *Optical Spectra*

A subsample of 11 galaxies in GOODS-N match to publicly available optical spectra from the Team Keck Treasury Redshift Survey (TKRS, Wirth et al. 2004), from which we use Hα and Hβ fluxes. The TKRS spectroscopic observations of GOODS-N were taken using DEIMOS on the Keck II telescope, with the spectra extracted using the DEEP2 Redshift Survey Team pipeline (Newman et al. 2013).

3. Paβ AS A STAR FORMATION RATE INDICATOR

Following the Kennicutt & Evans (2012) SFR relation for Hα and Hα/Paβ = 17.6 (assuming Case B recombination, $T = 10^4$ K, and $n_e = 10^4$ cm^{-3}; Osterbrock 1989), SFR is calculated from Paβ as:

$$\log(SFR_{Pa\beta})[M_\odot/yr] = \log[L(Pa\beta)] - 40.02 \quad (3)$$

In the following subsections, we compare Paβ SFRs measured from this equation with continuum and Hα SFR estimates.

### 3.1. *Paβ and Continuum SFR Indicators*

Here we compare Paβ SFRs with attenuation-corrected UV continuum SFRs to investigate hidden SFR and star formation histories (SFHs). The near-IR Paβ line is much less affected by dust attenuation than the UV continuum, and so Paβ can reveal star-forming regions that are otherwise obscured by dust in light of shorter wavelengths. In addition, Paβ (and other hydrogen emission lines) probes recent (<10 Myr) star formation, while the UV continuum probes star formation over longer (10-100 Myr) timescales (Kennicutt & Evans 2012). The comparison of Paβ and UV continuum SFRs yields an indicator of SFH stochasticity ("burstiness", e.g., Guo et al. 2012; Broussard et al. 2019).

Figure 4 shows the relation between Paβ luminosity and the attenuation-corrected UV SFR from the CANDELS/SHARDS multiwavelength catalog (Barro et al. 2019), with three panels color-coded by stellar mass, UV slope β, and V-band attenuation. Twelve of the galaxies in our sample have 24 μm detections, and their UV + IR ladder SFRs are shown as open symbols. Both SFRs correlate with stellar mass, as expected given the well-known star formation mass sequence of galaxies (Noeske et al. 2007; Whitaker et al. 2012), but there is more apparent scatter between the two SFR indicators in low-mass galaxies. The Paβ luminosity also tends to be greater than expected from the UV SFR in galaxies with steep UV slopes and high attenuation.

Figure 5 shows the "excess" Paβ SFR compared to the attenuation-corrected UV SFR, quantified as $\log \frac{SFR_{Pa\beta}}{SFR_{UV}^{corr}}$, with stellar mass, UV slope β, and A_V attenuation. Upward facing triangles indicate the Paβ 1σ detection limit for each galaxy: our Paβ-selected sample is generally only sensitive to galaxies with Paβ SFR similar to or greater than the UV SFR. We fit the detections (colored points) in each panel using linear regression, as implemented by the `linmix` (Kelly 2007) Python package, reporting the best-fit slope and its uncertainty in each panel.

There is a significant correlation (with a slope >3σ different from zero) between the excess Paβ SFR and the UV slope β (center panel of Figure 5), with galaxies of UV slope $\beta \gtrsim 0$ tending to have Paβ SFRs that are ~1-2 orders of magnitude greater than the UV SFR. These galaxies likely have dust-
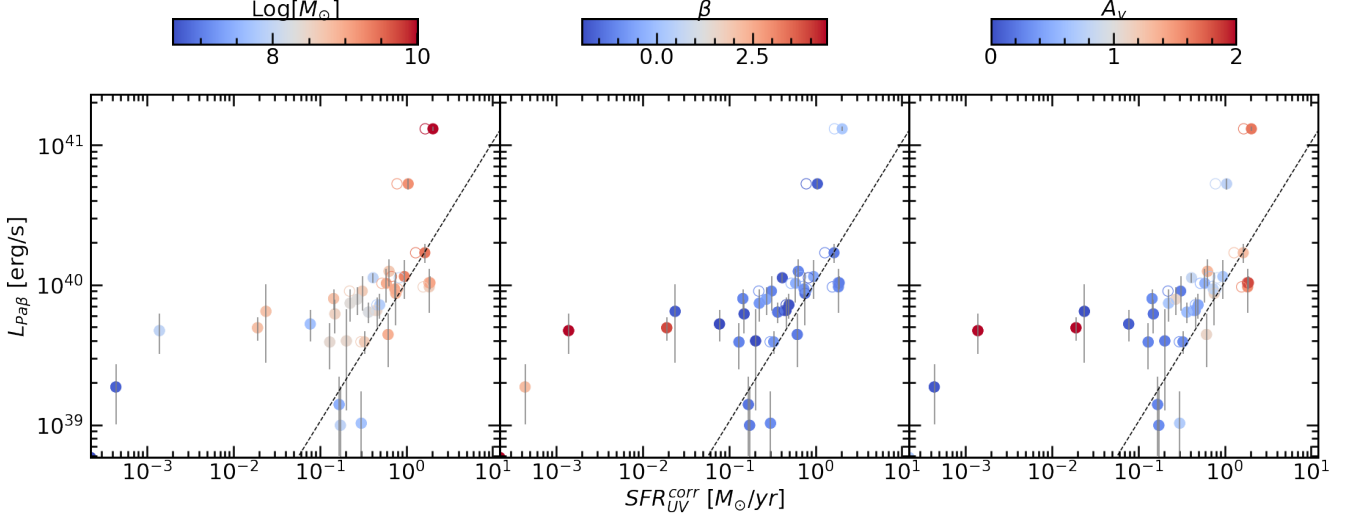
Figure 4. The relation between Paβ luminosity and continuum star formation rates for galaxies in our sample, color coded by mass (*left*), UV slope β (*center*), and continuum A_v (*right*). Filled circles correspond to the attenuation-corrected UV SFRs and empty circles correspond to UV + IR ladder SFRs for the twelve galaxies with well-detected IR emission (Barro et al. 2019). The gray line indicates the relation between Paβ luminosity and SFR calculated using Equation 3. The SFR measured from the Paβ luminosity is higher than the attenuation-corrected UV SFR in galaxies steep UV slopes and/or high attenuation, and there is more scatter between the two SFRs in galaxies with low stellar mass.
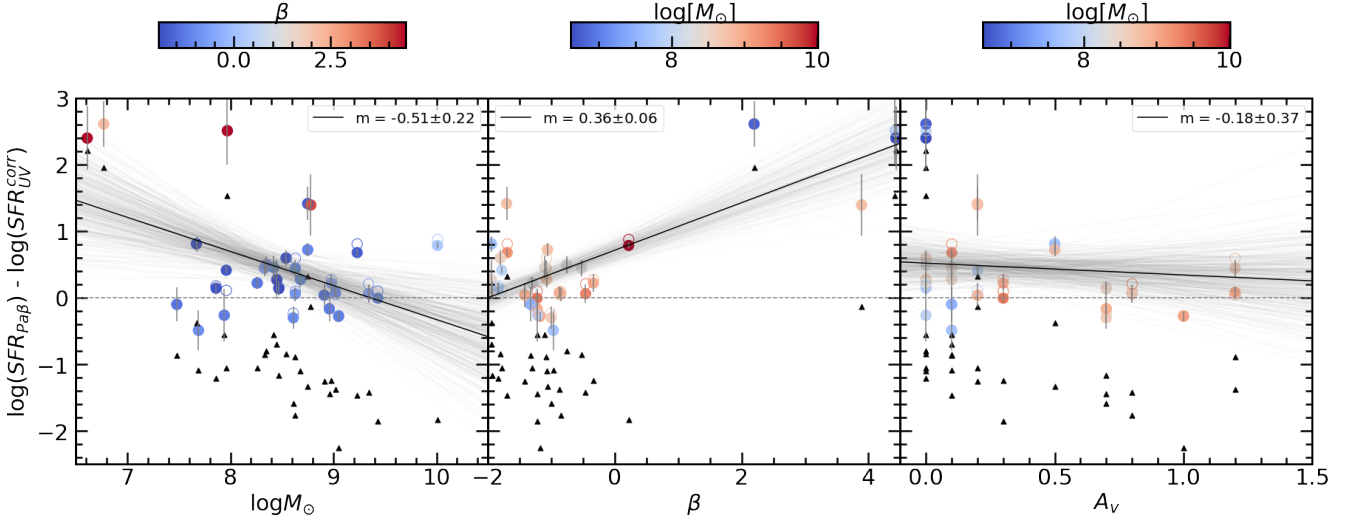

Figure 5. The log ratio of the Paβ and attenuation-corrected UV SFRs with stellar mass (*left*), UV slope β (*center*), and continuum A_v (*right*). Upward facing triangles indicate the 1σ detection limits of Paβ for each galaxy (using Equation 3). We fit each panel with a linear regression line, finding a significant correlation only in the center panel. Galaxies with steep UV slopes ($\beta \gtrsim 0$) tend to have much higher Paβ than UV SFRs, likely indicating star forming regions with high optical depths to UV emission but visible in Paβ emission. There is a marginal (2.3σ) correlation between Paβ excess and stellar mass, and the Paβ detection limits are consistent with higher scatter between the two SFRs (and burstier star formation histories) in low-mass galaxies.

enshrouded star formation that is not seen in UV light (for example, behind high optical depths) and is not accounted for by the attenuation correction. Paβ emission can escape these dusty star-forming regions that are optically thick to UV light, revealing star formation that is hidden at shorter wavelengths.

There is a marginal (2.3σ) correlation between Paβ excess and stellar mass (left panel of Figure 5). However the

significance of this fit may be influenced by the Paβ detection limits, which are mostly closer to a ratio of Paβ to UV SFRs of unity at low stellar mass. Our study is generally only sensitive to bursty star formation that occurred within the last 10 Myr, detectable as Paβ emission (with SFR$_{\text{Pa}\beta}$ > SFR$_{\text{UV}}$). In contrast, a burst of star formation occurring 10-100 Myr ago would lead to SFR$_{\text{Pa}\beta}$ < SFR$_{\text{UV}}$ that is generally not detectable in our sample (as shown by the
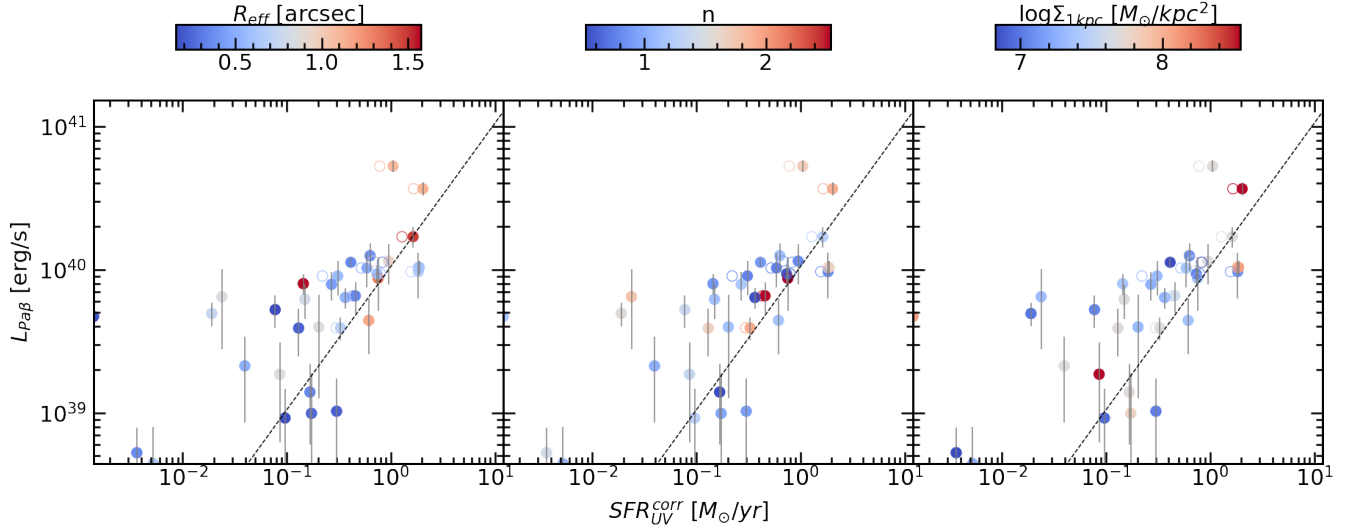
Figure 6. The relation between Paβ luminosity and attenuation-corrected UV star formation rates for galaxies in our sample, color coded by effective radius (*left*), Sérsic index (*center*) and Σ_{1kpc} (*right*). Filled circles correspond to the attenuation-corrected UV SFRs and empty circles correspond to UV + IR ladder SFRs for the twelve galaxies with well-detected IR emission (Barro et al. 2019). As in Figure 4, the gray line is the relationship between Paβ luminosity and SFR following Equation 3. None of these quantities appear to correlate with the ratio of Paβ to attenuation-corrected UV star formation rates, shown quantitatively in Figure 7.
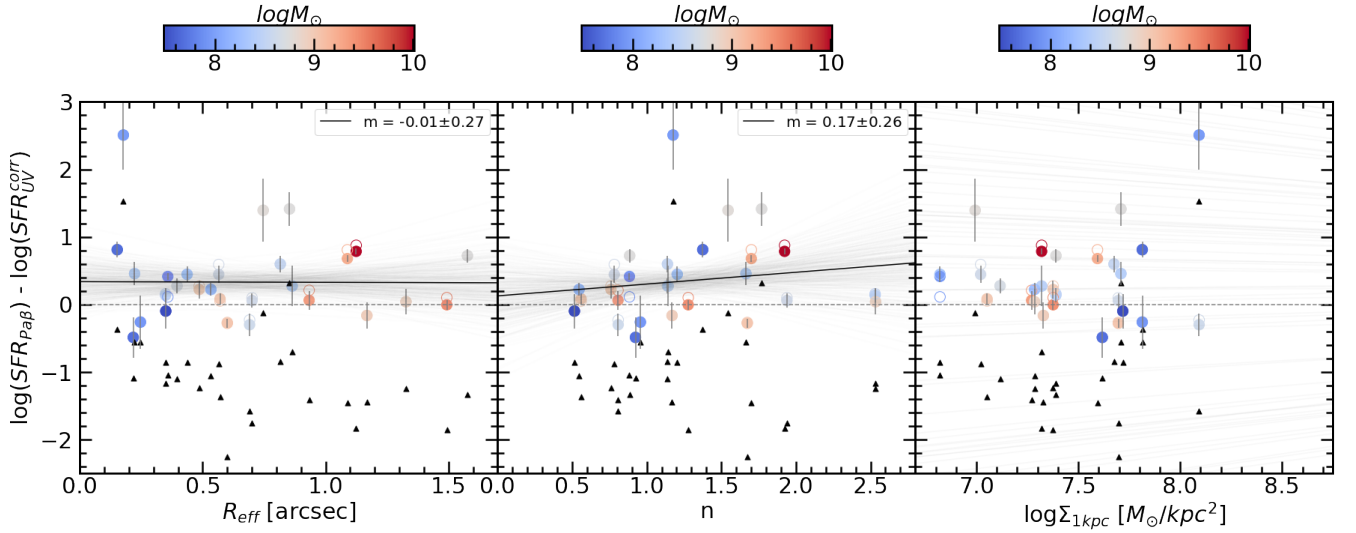
Figure 7. The log ratio of the Paβ and attenuation-corrected UV SFRs with galaxy effective radius (*left*) and Sérsic index (*right*). Upward facing triangles indicate the Paβ detection limits for each galaxy in our sample. The linear regression fits in each of the panels are all consistent with zero slope, indicating no correlation between these morphological indicators and the ratio of the Paβ/UV SFRs.

black upward facing triangles that indicate the Paβ flux limit for each galaxy in Figure 5). Thus we interpret the pattern of $\beta < 0$ galaxies in the left panel of Figure 5 as consistent with burstier star formation in low-mass galaxies. The Paβ detection limits are consistent with an undetected population of low-mass galaxies with $SFR_{Pa\beta} < SFR_{UV}$ that represent bursty star formation occurring >10 Myr ago, analogous to the larger number of $SFR_{Pa\beta} > SFR_{UV}$ galaxies representing bursts within the last 10 Myr. We discuss this further in Section 3.2.

Figure 6 shows the Paβ luminosity and attenuation-corrected UV SFR color-coded by galaxy size, Sérsic index (measured by van der Wel et al. 2012), and Σ_{1kpc} calculated from these values and their stellar masses. Figure 7 shows the log ratio of the Paβ to UV SFR versus the same morphology quantities. There are no significant correlations between the ratio of the two SFRs with galaxy size, Sérsic index, or Σ_{1kpc}. We conclude that galaxy morphology does not play a dominant role in the ratio between the Paβ and UV SFR of
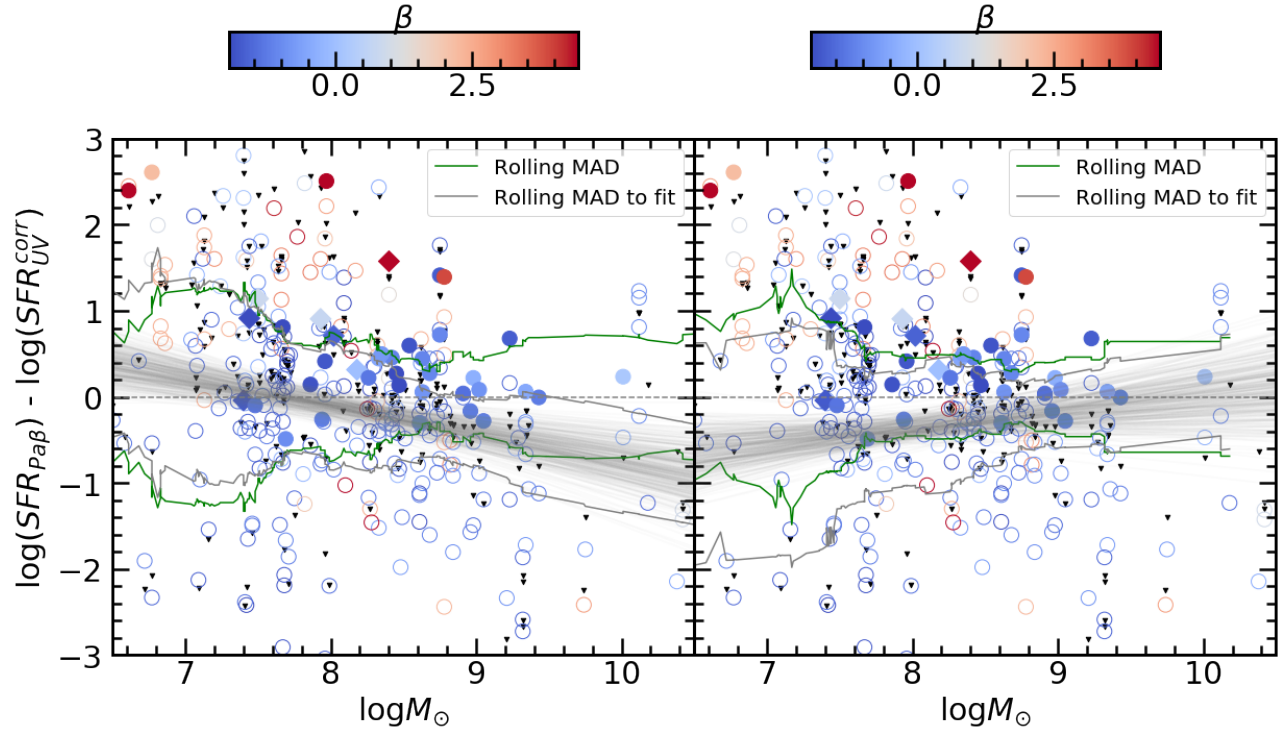
Figure 8. Survival analysis of the log ratio of Paβ and attenuation-corrected UV SFRs to stellar mass (similar to the left panel of Figure 5). The solid circles are the Paβ-detected objects in our sample (same as Figure 5) and diamonds indicate seven galaxies with marginal Paβ detections of $1 < SNR < 3$. Downward-facing black triangles represent the 1σ upper limits on all Paβ non-detections in CLEAR at $z < 0.287$, and open circles are randomly generated data from these non-detections using a half-normal distribution with standard deviation equal to the 1σ upper bounds. Both detections and the randomly generated survival analysis points are color-coded by UV slope β. Linear regression fits for the full sample of detections and non-detections (left) and the detections and non-detections with $\beta < 0$ (right) are shown as a gray family of lines. The green and gray lines show rolling median absolute deviations of the sample and survival analysis points about zero and about the mean best fit line, respectively. The survival analysis particularly populates the lower-left of the plot where we cannot detect Paβ-emitting galaxies. Scatter of the Paβ/UV SFR ratio increases at lower stellar mass, indicating burstier star formation histories.

a galaxy, i.e., bursty star formation histories and UV/nebular attenuation are not particularly tied to galaxy morphology.

3.2. *Burstier Star Formation at Low Stellar Mass*

The different star formation timescales probed by hydrogen recombination lines ($\sim$5 Myr) and UV continuum emission ($\sim$30 Myr) means that their comparison can be used to indicate the burstiness of star formation. Observations have long shown that the average ratio of Balmer-line to UV SFRs decreases at lower stellar mass (Sullivan et al. 2000; Boselli et al. 2009; Lee et al. 2009; Guo et al. 2016). The observations are best explained by an increasing importance of bursty of star formation occurring on timescales of tens of Myr, in which star formation that occurred 10-100 Myr ago is detected in UV emission but not in emission lines (Weisz et al. 2012; Hopkins et al. 2014; Shen et al. 2014; Sparre et al. 2017). But Broussard et al. (2019) notes that comparisons between Balmer-line and UV SFRs can be biased by uncertainties in the amount of dust attenuation (especially the UV shape of the attenuation law and the ratio of nebular to continuum attenuation).

The Paβ line should offer a clearer approach to measuring the burstiness of star formation since it is much less affected by attenuation than the Balmer lines. Our comparison between Paβ and UV SFRs in the left panel of Figure 5 indicates marginal (2.3σ) evidence for *higher* Paβ/UV SFR ratios at lower stellar masses. At face value, this is opposite the trend observed for the Hα/UV (and Hβ/UV) SFR ratio. However, our Paβ flux limits (upward facing triangles in Figure 5) generally preclude detection of low-mass galaxies with SFR(Paβ) < SFR(UV).

To investigate this further, we perform a survival analysis of the relation of the Paβ to attenuation-corrected UV SFR ratio to stellar mass in Figure 8. In addition to the real data from our sample (same as the left panel of Figure 5), we show the 1σ upper limits for all Paβ non-detections in CLEAR at $z < 0.287$ (downward facing triangles). We also show seven objects for which we have Paβ detection of $1 < \sigma < 3$ as diamonds. For each non-detection we randomly generate expectation values from a half-normal distribution with standard deviation equal to the 1σ upper bounds of each of the non-detections (open circles). We perform linear regression fits
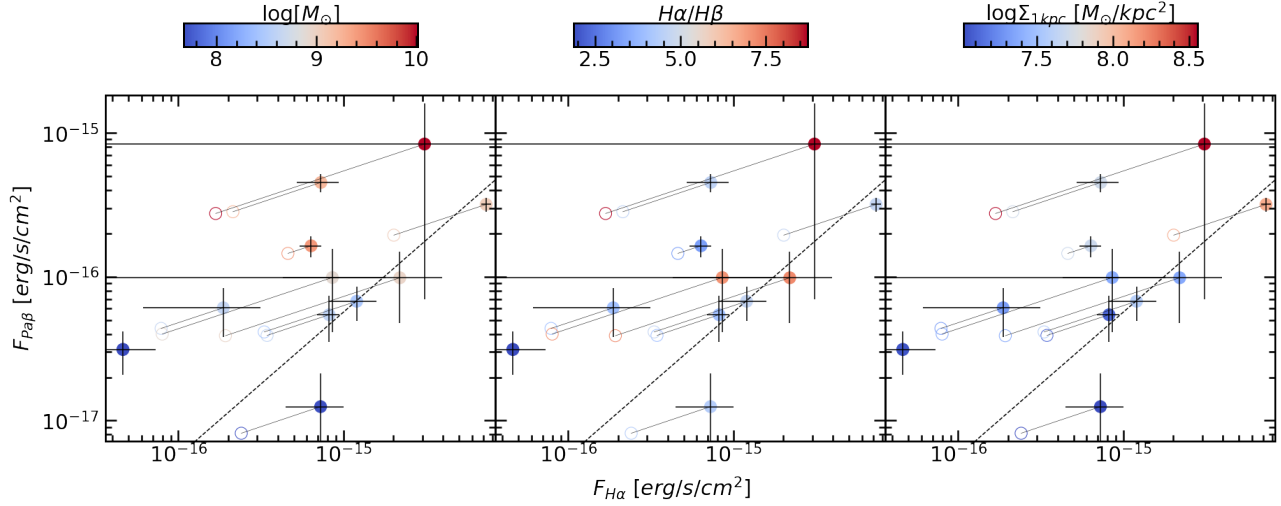
Figure 9. Paβ and Hα fluxes for the 11 galaxies in our sample with TKRS optical spectroscopy, color coded by stellar mass (*left*), Balmer decrement (*center*), and central density (Σ_{1kpc}) (*right*). The gray line indicates Paβ/Hα = 1/17.6, appropriate for Case B recombination with $T = 10^4$ K and $n_e = 10^4$ cm^{-3} (Osterbrock 1989). Open circles show uncorrected fluxes and filled circles are dust-corrected fluxes, calculated using the observed Balmer decrement and a Calzetti et al. (2000) attenuation curve. About half of the sample has dust-corrected ratios of Paβ/Hα that is significantly larger than the expected ratio, over a wide range of stellar mass, UV slope, and Balmer decrement. This suggests the Balmer decrement dust corrections are frequently insufficient and a significant fraction of the Hα emission may be hidden in regions behind high optical depths that are seen in Paβ emission.

both for the full sample of detections and randomly sampled non-detections (left panel of Figure 8) and again for detections and non-detections for relatively unattenuated galaxies with UV slope $\beta < 0$ (left panel of Figure 8). The green and gray lines show rolling median absolute deviations of the sample and survival analysis points about zero and about the mean best fit line, respectively.

The survival analysis shows that our observations are likely to include a large undetected population of low-Paβ/UV galaxies with a distribution (especially for galaxies with less UV attenuation) that is broadly consistent with previous work (cf. Figure 4 of Weisz et al. 2012). The scatter of the Paβ/UV SFR ratio increases at lower stellar mass, consistent with burstier star formation in low-mass ($M_\star < 10^8 M_\odot$) galaxies.

4. Paβ AND DUST ATTENUATION

4.1. *Paβ and Nebular Attenuation Indicators*

Because the recombination lines of hydrogen are insensitive to metallicity, temperature, and density, their ratios can be used to estimate attenuation in the line of sight. The most commonly used emission-line indicator of dust attenuation is Hα/Hβ. This rest-frame optical ratio only works for modestly attenuated galaxies, since it saturates at $A_V \sim 2$ (Groves et al. 2012). Even worse, Hα/Hβ attenuation measurements will entirely miss regions of the ISM that are optically thick to Hβ emission.

We compare the Paβ and Hα fluxes and SFRs to investigate if the near-IR emission line reveals star formation that is otherwise hidden in optical emission. Figure 9 shows the Paβ and Hα fluxes for galaxies in our sample that have optical

spectroscopy from TKRS in GOODS-N (Wirth et al. 2004). Open symbols show the observed fluxes, while filled symbols show the attenuation-corrected fluxes using the Balmer decrement and a Calzetti et al. 2000 attenuation model (assuming an intrinsic Case B Balmer decrement of Hα/Hβ = 2.86). The Paβ dust corrections are generally a factor of two or less, while the Hα dust corrections are often a factor of several or more. Even after dust-correcting according to the Balmer decrement, many of the galaxies have dust-corrected Paβ fluxes that are significantly greater than the expected ratio for Hα/Paβ (dashed lines in Figure 9). This suggests that the Balmer decrement is likely to underestimate the dust attenuation affecting Hα in many of our galaxies.

Figure 10 shows the log ratio of the Paβ and Hα SFRs. As in Figure 9, open symbols show the uncorrected SFRs and filled symbols are dust-corrected using the Balmer decrement and a Calzetti et al. (2000) attenuation model. There are no significant correlations between the Paβ/Hα ratio and the stellar mass, Balmer decrement, or central density (Σ_{1kpc}). High ratios of the attenuation-corrected Paβ/Hα are likely to occur if the attenuation is underestimated, i.e. if the Balmer decrement does not measure all of the attenuation. Figure 10 suggests that, at least within our small sample, Balmer decrements underestimate the attenuation in galaxies spanning a broad range of stellar mass, Balmer decrement, and galaxy central density.

Figure 11 directly compares the observed Paβ/Hα and Hα/Hβ ratios for the 11 galaxies in our CLEAR sample with optical spectra from TKRS (Wirth et al. 2004). The dotted line indicates the expected ratios for Calzetti et al.
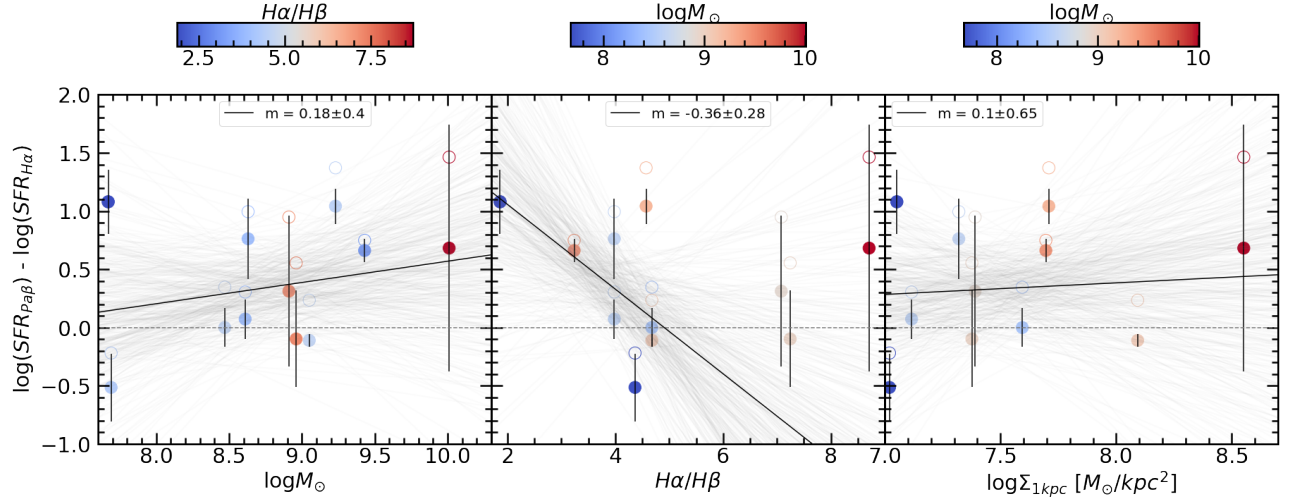
Figure 10. The relation of $SFR_{\mathrm{Pa}\beta}/SFR_{\mathrm{H\alpha}}$ to mass, size, and Balmer decrement, similar to Figure 4. We observe an excess of Paβ star formation for all but one object in our sample matching TKRS optical measurements. Open symbols show the observed fluxes, while filled symbols show the attenuation-corrected fluxes using the Balmer decrement and a Calzetti et al. 2000 attenuation model (assuming an intrinsic Balmer decrement of Hα/Hβ = 2.86). The Paβ dust corrections are generally a factor of two or less, while the Hα dust corrections are often a factor of several or more. Even after dust-correcting according to the Balmer decrement, many of the galaxies have dust-corrected Paβ fluxes that are significantly greater than the expected ratio for Hα/Paβ. This indicates that Paβ picks up star formation missed by optical emission-line SFR indicators.
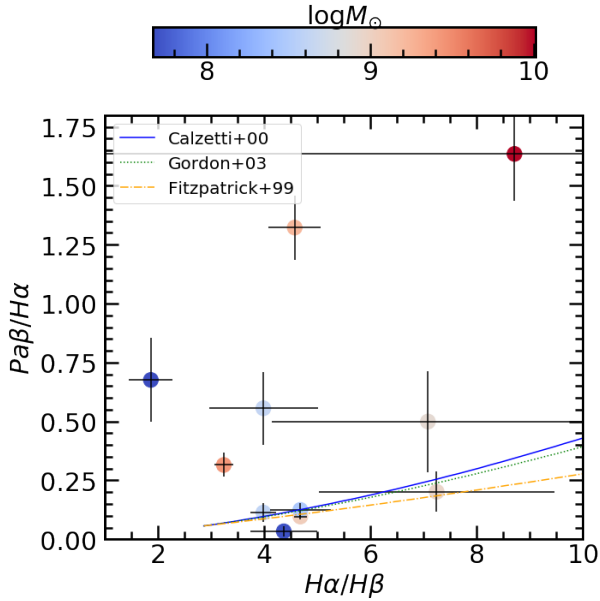
Figure 11. Paβ/Hα and Hα/Hβ ratios for 11 galaxies in the our sample with public optical spectroscopy from TKRS (Wirth et al. 2004). Our sample includes at least one highly dusty galaxy (in the upper right) for which Hα/Hβ is saturated and cannot reliably measure dust attenuation. The blue, green, and orange lines indicate the expected ratios using intrinsic Case B ratios of Hα/Hβ = 2.86 and Paβ/Hα = 1/17.6, and Calzetti et al. (2000) Gordon et al. (2003), and Fitzpatrick (1999) attenuation models. Eight of the 11 points have line ratios within 3σ consistent with the expectation.

(2000), SMC (Gordon et al. 2003), and Milky Way (Fitzpatrick 1999) attenuation models, using intrinsic Case B ra-

tios of Hα/Hβ = 2.86 and Paβ/Hα = 1/17.6. Most (8/11) galaxies have line ratios that are broadly (within $<3\sigma$) consistent with the expectation, but 3 have significantly larger Paβ/Hα ratios than expected from their Hα/Hβ ratios. As in Figures 9 and 10, we interpret these galaxies as having Hα/Hβ ratios that underestimate the true attenuation. In the galaxy with the highest Hα/Hβ (upper right of Figure 11, this is somewhat expected since the Balmer decrement is likely to be saturated (within gas that is optically thick to Hβ emission). The other 2 galaxies might similarly have Balmer decrements that probe only optically thin gas, with an additional ISM component that is optically thick to Hβ (and possibly Hα) but optically thin to Paβ emission.

The small size of our sample, with only 11 galaxies that have both rest-optical spectroscopy for Hβ and Hα along with rest-IR spectroscopy for Paβ, makes it unclear if our observations are representative of the nebular attenuation properties in the broader population of galaxies. But we find evidence that at least some galaxies – across a range of stellar mass, observed Hα/Hβ, and Σ_1 – have Balmer decrements that underestimate the attenuation and miss star formation that is otherwise revealed by Paβ.

4.2. Nebular Paβ/Hα and Continuum Attenuation

Figure 12 compares the nebular attenuation measured by Paβ/Hα with the continuum V-band attenuation A_V and the UV slope β. In the left panel we also show Calzetti et al. (2000), Milky Way (Fitzpatrick 1999), and SMC (Gordon et al. 2003) attenuation curves for a stellar to nebular attenuation ratio of 0.44, as well as the Calzetti et al. (2000) curve
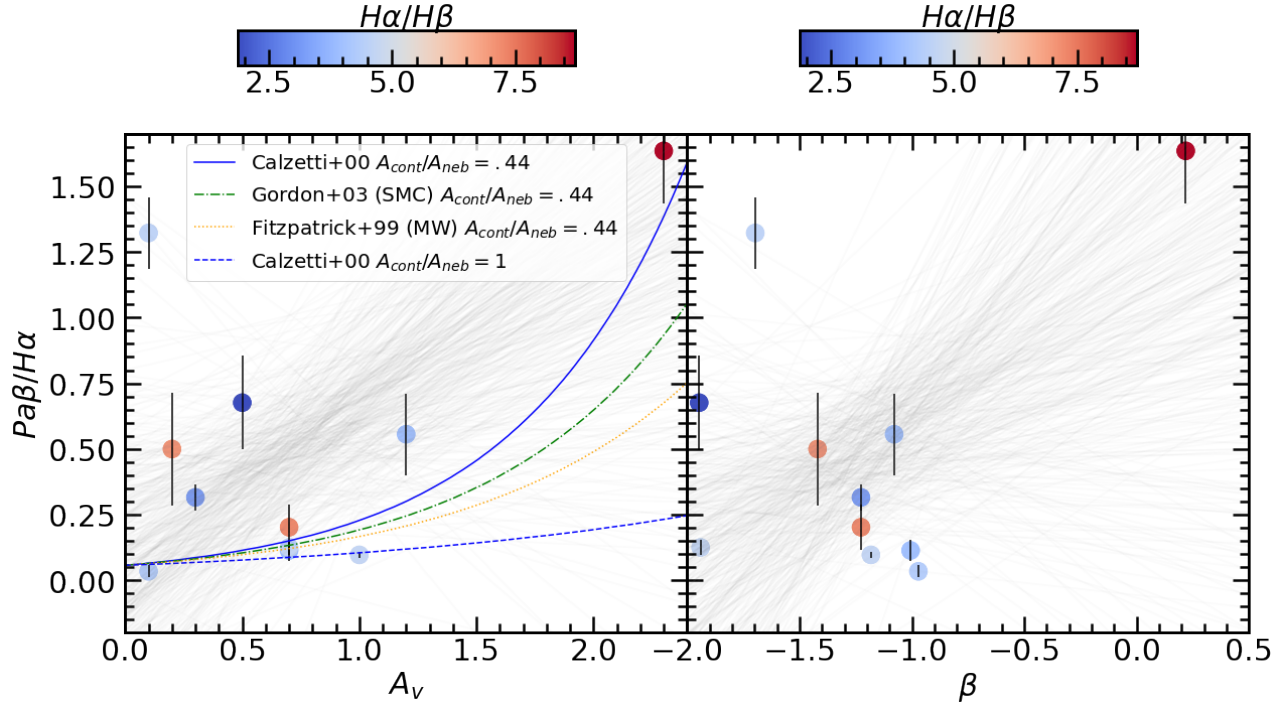
Figure 12. The relation between Paβ/Hα ratios and the 3D-HST A_v (Momcheva et al. 2016) and Barro et al. (2019) UV slope β for 11 galaxies in the our sample with public optical spectroscopy from TKRS (Wirth et al. 2004). Our sample includes at least one highly dusty galaxy (in the upper right) for which Hα/Hβ is saturated and cannot reliably measure dust attenuation. The left panel shows Calzetti et al. (2000), Gordon et al. (2003), and Fitzpatrick (1999) attenuation curves with a stellar to nebular attenuation ratio of 0.44, along with another Calzetti et al. (2000) attenuation curve with a stellar to nebular attenuation ratio of 1.

for equal stellar and nebular attenuation. All models assume an intrinsic Paβ/Hα = 1/17.6. In both panels the nebular and continuum attenuation are broadly correlated, but with large scatter that results in best-fit regression lines with slopes that are only marginally ($<3\sigma$) different from zero. Most (8/11) of the galaxies have observed Paβ/Hα ratios that are $<3\sigma$ consistent with the dotted line, albeit with significant excess scatter that suggests a large diversity of stellar to nebular attenuation ratios. Three of the galaxies have significantly larger Paβ/Hα ratios than expected for their A_V, and these are the same three galaxies with larger Paβ/Hα than expected for their Balmer decrements. These galaxies are likely to have measured A_V values that underestimates the attenuation, and/or have enshrouded star-forming regions that are optically thick to optical line and continuum emission but apparent in the near-IR Paβ line.

Figure 13 shows the same relation as the left panel of Figure 12 with the points shown by the F125W thumbnails from CLEAR. The dustiest galaxy with the highest Paβ/Hα and A_V (and also the highest Hα/Hβ) is an edge-on galaxy with a dust lane, and many of the other high-Paβ/Hα galaxies are similarly edge-on disks. This suggests that inclined disk galaxies may be especially prone to having optical emission lines and continuum that is obscured by optically thick
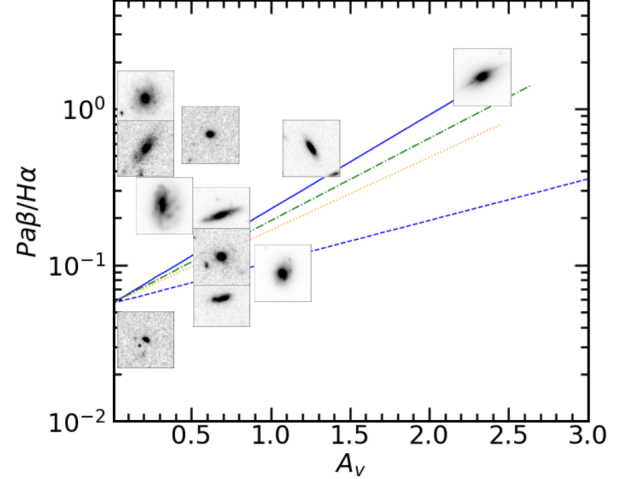
Figure 13. Thumbnail images of the 11 galaxies in our sample with TKRS spectroscopy, overlaid on their log(Paβ/Hα) ratios and continuum A_V. The same 4 attenuation curves are plotted as in Figure 12. Many of the galaxies with high Paβ/Hα ratios are edge-on disks, and the dustiest galaxy (in the upper right) has an apparent dust lane.

dust, with significant amounts of star formation revealed only through less attenuated lines like Paβ.

In this section we have discussed the advantages of using comparisons of Paβ to emission-line tracers and continuum

indicators to show dust attenuation missed by these other methods. We showed that the ratio Paβ/Hα is a superior attenuation indicator compared to the traditionally used Balmer decrement.

5. SUMMARY AND CONCLUSIONS

We have analyzed a sample of 32 low redshift ($z < 0.287$) Paβ emitting galaxies. The galaxies of our sample have been selected such that the *HST* G141 grism detects Paβ with an observed frame wavelength of $\lambda \leq 16500$Å with a signal-to-noise ratio of $\sigma \geq 3$, and we additionally include 11 galaxies with reliable spectroscopic redshifts from other lines (from either ground-based optical spectroscopy or from Hα emission in the G102 spectrum) that have Paβ detected with SNR > 1. We also required that the objects in our sample have minimally contaminated 2-D spectra. This sample comprises approximately 11% of all CLEAR galaxies in this redshift range.

Our study of these Paβ emitting galaxies provides two primary findings. First, we conclude that Paβ is a superior indicator of star formation rates and star formation histories when compared to traditional SFR indicators such as Hα flux and continuum emission. Paβ as an indicator of SFR serves as a solution to the issues with dust attenuation experienced by SFRs based on optical emission line tracers such as Hα This method of finding SFRs also probes a shorter timescale than probed by continuum emission, so we can draw conclusions about the star formation histories of galaxies by comparing the two

Our second major finding shows Paβ/Hα ratios serve as a superior indicator of dust attenuation when we compare these to the Balmer decrement and continuum attenuation estimates. Paβ/Hα has the same insensitivity to nuisance pa-

rameters such as metallicity, temperature, and density as the Balmer decrement, but does not saturate as easily. Paβ/Hα also does not risk miscalculating attenuation for ISM regions optically thick to Hβ.

Our results motivate future IR observations of Paschen series lines for measuring star formation rate. The *James Webb Space Telescope* (*JWST*) will reach a flux limit that is an order of magnitude fainter than our CLEAR data for similar exposure times, enabling detection of fainter Paschen-line emission in low stellar mass galaxies where our work has to rely on survival analysis. In addition, the broad 1-5 μm spectroscopic coverage of *JWST* includes the Paα line, which is twice as bright than Paβ, for galaxies over $z < 1.65$. Future *JWST* observations of Paschen-line emission in galaxies are likely to reveal a much more complete picture of star formation and bursty formation histories, especially in galaxies with significant dust attenuation.

Table 1. Sample characteristics and derived quantities

Field	ID	RA	Dec	Redshift[i]	Stellar Mass[ii]	Paβ Flux	SFR$_{UV}^{corr}$[iii]	SFR$_{ladder}$[iii]	β[iii]	A$_v$[ii]	R$_{eff}$[iv]	Sérsic index[iv]	Σ$_{1kpc}$	F435W - F775W[iii]
		Deg	Deg		log$M_\odot$	10^{-17} erg s^{-1} cm^{-2}	$M_\odot/yr$	$M_\odot/yr$		mag	''		$M_\odot\ kpc^{-2}$	mag
GN1	37683	189.30609	62.36035	0.2755	8.61	3.9 ± 1.4	1.8 ± 0.3	1.57	-1.01	0.7	0.69 ± 0.02	0.81 ± 0.07	7.12	0.97
GN2	19221	189.20126	62.24070	0.1389	9.05	19.4 ± 2.1	1.9 ± 0.2	1.83	-1.18	1.0	0.600 ± 0.009	1.67 ± 0.05	8.09	0.91
GN2	15610	189.21272	62.22242	0.2008	9.43	14.5 ± 2.3	1.64 ± 0.07	1.28	-1.23	0.3	1.49 ± 0.07	1.3 ± 0.1	7.70	1.15
GN2	18157	189.18229	62.23246	0.2013	8.96	3.9 ± 1.6	0.61 ± 0.095	1.11	-1.23	0.7	1.2 ± 0.2	1.2 ± 0.4	7.38	1.26
GN2	21693	189.23252	62.24847	0.28 ± 0.02	8.75	2.5 ± 1.4	0.024 ± 0.002	0.03	-1.71	0.2	0.9 ± 0.3	2 ± 1	7.33	2.03
GN3	34456	189.33981	62.32429	0.2113	10.01	27.5 ± 2.9	2.0 ± 0.2	1.66	0.22	2.3	1.1 ± 0.2	1.9 ± 0.5	8.55	2.20
GN3	34157	189.20683	62.32120	0.2755	9.23	28.3 ± 2.7	1.05 ± 0.09	0.78	-1.70	0.1	1.1 ± 0.1	1.7 ± 0.4	7.71	1.21
GN3	33397	189.17547	62.31435	0.25 ± 0.01	9.34	6.2 ± 1.9	0.95 ± 0.08	0.68	-0.46	0.8	0.9 ± 0.07	0.8 ± 0.1	7.68	1.66
GN3	33511	189.23455	62.31477	0.2535	8.63	4.4 ± 1.2	0.31 ± 0.04	0.22	-1.08	1.2	0.6 ± 0.1	0.8 ± 0.6	7.32	1.53
GN3	34368	189.33853	62.32097	0.2311	8.47	4.1 ± 1.0	0.46 ± 0.01	0.44	-1.94	0.7	0.3 ± 0.2	2.5 ± 3.2	7.59	0.92
GN3	34077	189.21093	62.31770	0.25 ± 0.01	8.33	4.1 ± 0.9	0.27 ± 0.04	1.10	-0.53	0.1	0.44 ± 0.03	1.2 ± 0.2	7.27	1.20
GN3	35455	189.33207	62.32867	0.2468	7.69	0.8 ± 0.6	0.30 ± 0.04	0.71	-0.97	0.1	0.22 ± 0.03	0.9 ± 0.5	7.02	0.64
GN4	24611	189.35906	62.26414	0.2662	8.91	4.0 ± 1.6	0.76 ± 0.10	1.12	-1.42	0.2	1.3 ± 0.1	2.5 ± 0.4	7.39	1.16
GN5	33249	189.20772	62.31110	0.2305	7.67	3.1 ± 0.8	0.078 ± 0.007	0.08	-1.95	0.5	0.2 ± 0.03	1.4 ± 0.7	7.05	0.83
GS2	45518	53.15409	-27.69793	0.282 ± 0.005	8.68	4.9 ± 1.1	0.63 ± 0.09	1.33	-1.08	0.0	0.395 ± 0.004	1.14 ± 0.03	7.12	0.98
GS2	49771	53.14058	-27.67298	0.27 ± 0.05	7.97	1.9 ± 0.6	0.001 ± 0.002	4.64	4.42	0.0	0.177 ± 0.004	1.8 ± 0.1	8.09	1.49
GS3	37720	53.13911	-27.73031	0.1031	8.63	13.4 ± 2.5	0.33 ± 0.05	0.30	-0.85	0.8	0.701 ± 0.002	1.94 ± 0.01	7.70	1.03
GS3	41882	53.17335	-27.71496	0.2501	8.98	5.9 ± 1.6	0.59 ± 0.08	0.52	-0.34	0.3	0.486 ± 0.002	0.76 ± 0.01	7.38	1.34
GS3	42593	53.15580	-27.71195	0.24 ± 0.02	8.42	2.1 ± 0.8	0.13 ± 0.02	0.27	-1.11	0.1	0.223 ± 0.003	1.66 ± 0.04	7.71	1.42
GS3	35433	53.14153	-27.74583	0.26 ± 0.02	8.45	1.9 ± 1.3	0.20 ± 0.02	0.22	-1.95	0.1	0.86 ± 0.02	1.14 ± 0.04	7.32	1.12
GS3	39564	53.17732	-27.72556	0.25 ± 0.06	6.77	0.9 ± 0.4	0.0004 ± 0.0003	0.06	2.20	0.0	0.0180 ± 0.0004	0.41 ± 0.03	7.02	1.99
GS4	27438	53.19393	-27.78580	0.1280	8.75	23.3 ± 3.9	0.14 ± 0.02	0.31	-1.06	0.5	1.577 ± 0.007	0.885 ± 0.007	7.39	1.28
GS4	27549	53.14471	-27.78544	0.2467 ± 0.0007	7.96	5.9 ± 0.4	0.41 ± 0.04	0.83	-1.79	0.2	0.3578 ± 0.0008	0.884 ± 0.006	6.82	0.71
GS4	26639	53.14212	-27.78670	0.2270	9.02	5.9 ± 0.9	0.74 ± 0.09	0.79	-0.87	1.2	0.5704 ± 0.0003	0.5596 ± 0.0009	7.05	1.39
GS4	26696	53.19564	-27.78777	0.2270	7.86	4.6 ± 0.9	0.49 ± 0.04	0.46	-1.84	0.0	1.02 ± 0.03	8.0 ± 0.3	7.62	0.35
GS4	25632	53.15464	-27.79324	0.23 ± 0.01	8.26	3.9 ± 0.6	0.37 ± 0.05	0.60	-1.30	0.0	0.533 ± 0.001	0.546 ± 0.005	7.29	0.77
GS4	26646	53.18153	-27.78797	0.2122	7.48	1.2 ± 0.7	0.17 ± 0.02	0.27	-1.33	0.1	0.350 ± 0.002	0.52 ± 0.01	7.72	0.52
GS4	27535	53.17032	-27.78526	0.277 ± 0.006	7.94	0.4 ± 0.4	0.17 ± 0.02	0.30	-1.22	0.0	0.247 ± 0.002	0.96 ± 0.02	7.81	0.91
GS4	26559	53.14984	-27.78744	0.244 ± 0.004	6.61	0.3 ± 0.2	0.0002 ± 0.0002	0.69	4.43	0.0	0.0216 ± 0.0004	1.50 ± 0.07	7.29	2.22
GS5	43071	53.12259	-27.70791	0.16 ± 0.02	8.78	6.8 ± 1.3	0.02 ± 0.02	30.31	3.89	0.2	0.746 ± 0.005	1.55 ± 0.02	6.99	1.73
ERSPRIME	39634	53.07824	-27.72492	0.19 ± 0.02	8.54	5.7 ± 1.5	0.150 ± 0.006	0.17	-1.81	0.0	0.82 ± 0.01	1.14 ± 0.03	7.68	1.11
ERSPRIME	44465	53.05034	-27.70341	0.243 ± 0.005	8.35	4.0 ± 1.0	0.22 ± 0.03	0.69	-0.76	0.0	0.43 ± 0.02	8.0 ± 0.4	6.97	1.22

[i] Objects with spectroscopic redshifts are quoted without redshift uncertainty. Objects only with grism redshifts are quoted with uncertainties.

[ii] From the 3D-HST catalog Skelton et al. (2014)

[iii] From the CANDELS/SHARDS catalog Barro et al. (2019)

[iv] From the GALFIT catalog van der Wel et al. (2012)

REFERENCES

Alonso-Herrero, A., Rieke, G. H., Rieke, M. J., et al. 2006, ApJ, 650, 835

Barro, G., Pérez-González, P. G., Cava, A., et al. 2019, ApJS, 243, 22

Boselli, A., Boissier, S., Cortese, L., et al. 2009, ApJ, 706, 1527

Brammer, G. B., van Dokkum, P. G., & Coppi, P. 2008, ApJ, 686, 1503

Broussard, A., Gawiser, E., Iyer, K., et al. 2019, ApJ, 873, 74

Bruzual, G., & Charlot, S. 2003, MNRAS, 344, 1000

Calzetti, D., Armus, L., Bohlin, R. C., et al. 2000, ApJ, 533, 682

Calzetti, D., Kennicutt, R. C., Engelbracht, C. W., et al. 2007, ApJ, 666, 870

Chabrier, G. 2003, Publications of the Astronomical Society of the Pacific, 115, 763

Estrada-Carpenter, V., Papovich, C., Momcheva, I., et al. 2019, ApJ, 870, 133

Finkelstein, K. D., Papovich, C., Finkelstein, S. L., et al. 2011, ApJ, 742, 108

Fitzpatrick, E. L. 1999, PASP, 111, 63

Gordon, K. D., Clayton, G. C., Misselt, K. A., Land olt, A. U., & Wolff, M. J. 2003, ApJ, 594, 279

Grogin, N. A., Kocevski, D. D., Faber, S. M., et al. 2011, ApJS, 197, 35

Groves, B., Brinchmann, J., & Walcher, C. J. 2012, MNRAS, 419, 1402

Guo, Y., Giavalisco, M., Cassata, P., et al. 2012, ApJ, 749, 149

Guo, Y., Rafelski, M., Faber, S. M., et al. 2016, ApJ, 833, 37

Hinshaw, G., Larson, D., Komatsu, E., et al. 2013, ApJS, 208, 19

Hopkins, P. F., Kereš, D., Oñorbe, J., et al. 2014, MNRAS, 445, 581

Kelly, B. C. 2007, ApJ, 665, 1489

Kennicutt, Robert C., J. 1998, ApJ, 498, 541

Kennicutt, R. C., & Evans, N. J. 2012, ARA&A, 50, 531

Koekemoer, A. M., Faber, S. M., Ferguson, H. C., et al. 2011, ApJS, 197, 36

Kriek, M., van Dokkum, P. G., Labbé, I., et al. 2009, ApJ, 700, 221

Lee, J. C., Gil de Paz, A., Tremonti, C., et al. 2009, ApJ, 706, 599

Momcheva, I. G., Brammer, G. B., van Dokkum, P. G., et al. 2016, ApJS, 225, 27

Newman, J. A., Cooper, M. C., Davis, M., et al. 2013, ApJS, 208, 5

Noeske, K. G., Weiner, B. J., Faber, S. M., et al. 2007, ApJL, 660, L43

Osterbrock, D. E. 1989, Astrophysics of gaseous nebulae and active galactic nuclei

Papovich, C., Rudnick, G., Rigby, J. R., et al. 2009, ApJ, 704, 1506

Peng, C. Y., Ho, L. C., Impey, C. D., & Rix, H.-W. 2010, AJ, 139, 2097

Pérez-González, P. G., Cava, A., Barro, G., et al. 2013, ApJ, 762, 46

Salim, S., & Narayanan, D. 2020, arXiv e-prints, arXiv:2001.03181

Sérsic, J. L. 1968, Atlas de Galaxias Australes

Shen, S., Madau, P., Conroy, C., Governato, F., & Mayer, L. 2014, ApJ, 792, 99

Shipley, H. V., Papovich, C., Rieke, G. H., Brown, M. J. I., & Moustakas, J. 2016, ApJ, 818, 60

Skelton, R. E., Whitaker, K. E., Momcheva, I. G., et al. 2014, ApJS, 214, 24

Sparre, M., Hayward, C. C., Feldmann, R., et al. 2017, MNRAS, 466, 88

Sullivan, M., Treyer, M. A., Ellis, R. S., et al. 2000, MNRAS, 312, 442

van der Wel, A., Bell, E. F., Häussler, B., et al. 2012, ApJS, 203, 24

Weisz, D. R., Johnson, B. D., Johnson, L. C., et al. 2012, ApJ, 744, 44

Whitaker, K. E., Kriek, M., van Dokkum, P. G., et al. 2012, ApJ, 745, 179

Wirth, G. D., Willmer, C. N. A., Amico, P., et al. 2004, AJ, 127, 3121

Wuyts, S., Förster Schreiber, N. M., Lutz, D., et al. 2011, ApJ, 738, 106

Table 2. TKRS spectroscopy and attenuation-corrected fluxes.

Field	ID	Observed Flux 10^{-17} erg s^{-1} cm^{-2}			Attenuation-Corrected Flux 10^{-17} erg s^{-1} cm^{-2}		
		Paβ	Hα	Hβ	Paβ	Hα	Hβ
GN1	37683	3.9 ±1.4	34.4 ±1.0	8.6 ±0.4	5.4 ±1.9	81.8 ±13.0	28.6 ±6.4
GN2	19221	19.4 ±2.1	201.3 ±1.7	43.0 ±1.0	31.8 ±3.6	729.0 ±48.7	255.0 ±24.1
GN2	15610	14.5 ±2.3	46.0 ±1.1	14.2 ±0.7	16.4 ±2.8	63.6 ±9.5	22.2 ±4.7
GN2	18157	3.9 ±1.6	19.3 ±1.6	2.7 ±0.8	9.8 ±5.1	219.0 ±176.0	76.6 ±87.7
GN3	34456	85.4 ±2.8	14.7 ±0.9	1.7 ±1.5	83.6 ±76.6	309.0 ±739.0	108.0 ±370.0
GN3	34157	28.3 ±2.7	21.4 ±0.9	4.7 ±0.5	45.2 ±6.5	72.9 ±20.8	25.5 ±10.3
GN3	33511	4.4 ±1.2	7.9 ±0.5	2.0 ±0.5	6.1 ±2.3	18.7 ±12.6	6.5 ±6.3
GN3	34368	4.1 ±1.0	33.1 ±1.0	7.1 ±0.8	6.8 ±1.8	120.0 ±38.5	41.9 ±19.2
GN3	35455	0.8 ±0.6	24.0 ±1.5	5.5 ±0.7	1.2 ±0.9	72.6 ±27.8	25.4 ±13.7
GN4	24611	4.0 ±1.6	8.0 ±1.0	1.1 ±0.4	9.9 ±5.8	85.5 ±93.6	29.9 ±46.5
GN5	33249	3.1 ±0.8	4.6 ±0.3	2.5 ±0.5	3.1 ±1.0	4.6 ±2.7	2.5 ±2.1

NOTE—Attenuation-corrected fluxes are calculated using a Calzetti et al. (2000) attenuation model assuming an intrinsic Case B recombination Balmer decrement of Hα/Hβ = 2.86.